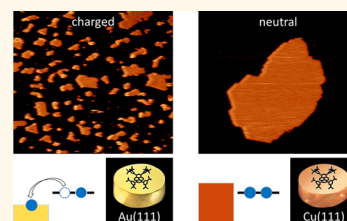# Anomalous Coarsening Driven by Reversible Charge Transfer at Metal—Organic Interfaces

Ada Della Pia,[†] Massimo Riello,[‡] Andrea Floris,[‡] Daphne Stassen,[§] Tim S. Jones,[†] Davide Bonifazi,*,[§,‖] Alessandro De Vita,*,[‡,∞] and Giovanni Costantini*,[†]

[†]Department of Chemistry, University of Warwick, Gibbet Hill Road, Coventry CV4 7AL, United Kingdom, [‡]Department of Physics, King's College London, Strand, London WC2R 2LS, United Kingdom, [∞]Department of Engineering and Architecture, University of Trieste, Trieste, Italy I-34127, [§]Namur Research College (NARC) and Department of Chemistry, University of Namur (UNamur), Namur, Belgium B-5000, and [‖]Department of Pharmaceutical and Chemical Sciences and INSTM UdR di Trieste, University of Trieste, Trieste, Italy I-34127

ABSTRACT The unique electronic properties and functional tunability of polycyclic aromatic hydrocarbons have recently fostered high hopes for their use in flexible, green, portable, and cheap technologies. Most applications require the deposition of thin molecular films onto conductive electrodes. The growth of the first few molecular layers represents a crucial step in the device fabrication since it determines the structure of the molecular film and the energy level alignment of the metal—organic interface. Here, we explore the formation of this interface by analyzing the interplay between reversible molecule—substrate charge transfer, yielding intermolecular repulsion, and van der Waals attractions in driving the molecular assembly. Using a series of *ad hoc* designed molecules to balance the two effects, we combine scanning tunnelling microscopy with atomistic simulations to study the self-assembly behavior. Our systematic analysis identifies a growth mode characterized by anomalous coarsening that we anticipate to occur in a wide class of metal—organic interfaces and which should thus be considered as integral part of the self-assembly process when depositing a molecule on a conducting surface.

KEYWORDS: charge transfer · metal—organic interfaces · interfacial dipoles · self-assembly at surfaces · polycyclic aromatic hydrocarbons

Surface dipoles at metal—organic interfaces regulate the alignment between the energy levels of active organic materials and the electrode Fermi level, playing a crucial role in the charge injection properties and eventually in the efficiency of (opto-)electronic devices.[1,2] Particularly relevant are the interfacial dipoles generated by charge transfer (CT) processes, since they can occur for a very wide class of π-conjugated molecular modules and are, at the same time, the most difficult to predict and control. Derivatives of all-carbon polycyclic aromatic hydrocarbons (PAHs) are particularly suited to act as donor molecular modules since their gas phase ionization energies are comparable to the Fermi levels of several metals.[3–5] To achieve a model system suitable to investigate the influence of CT processes on the supramolecular assembly at metal—organic interfaces, we designed a new pyrene derivative, tetra[1,3-di(*tert*-butyl)phenyl]pyrene (TBP)

(see Scheme 1a and Supporting Information), and studied its interaction with single-crystal metal substrates of different work functions, namely Au(111) and Cu(111). The coherence of our findings was demonstrated by analyzing the assembly behavior of two additional programmed tetra-legged PAHs, 1,3,6,8-tetramesitylpyrene (TMP) and 2,5,8,11-tetrakis(3,5-di*tert*-butylphenyl)perylene (TPPr) (Scheme 1) that, featuring a different adsorption height with respect to TBP, selectively enable or inhibit interfacial charge transfer.
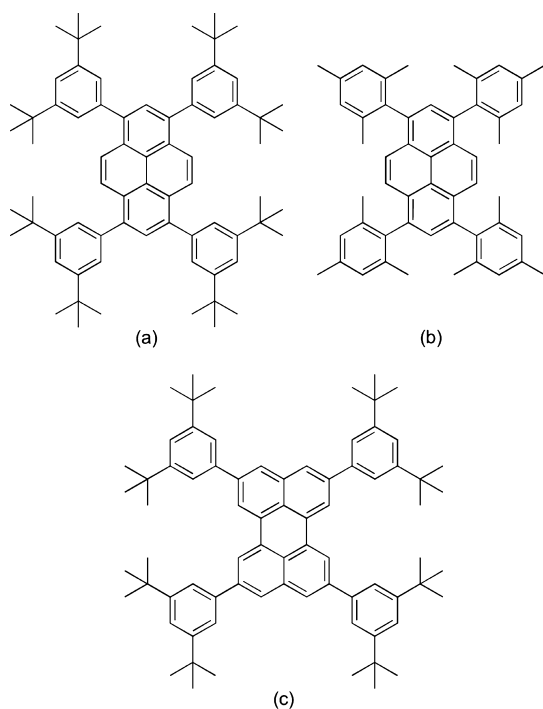
RESULTS AND DISCUSSION

Figure 1a shows the relaxed gas phase structure of the TBP molecule as obtained from density functional theory (DFT) calculations. The stable configuration has a three-dimensional structure with an almost flat central aromatic core and four conformationally free peripheral phenyl rings. Its calculated ionization potential is 6.15 eV, with

© 2014 American Chemical Society

Scheme 1. Schematic representation of the investigated molecules (a) TBP, (b) TMP, and (c) TPPr.

the HOMO mainly localized within the core but extending also into the 1,3-di(*tert*-butyl)phenyl rings (Figure SI-4). TBP molecules were deposited by thermal sublimation in ultra high vacuum on Cu(111) and Au(111) surfaces kept at room temperature, and their self-assembly behavior was investigated by low temperature scanning tunnelling microscopy (LT-STM). On both substrates, single TBP molecules appear as eight bright bulges, each corresponding to the *tert*-butyl residues, with the four central ones being higher than the others (Figure 1c). These observations are consistent with the DFT-calculated adsorption configuration which, for both Cu(111) and Au(111), predicts that the pyrene core is significantly deformed in a pronounced saddle shape, while the phenyl rings are rotated in the plane due to the hindrance from the substrate (Figure 1b). This concave adsorption geometry is associated with an intrinsic electrostatic dipole of 0.90 and 1.53 D for TBP on

Cu(111) and Au(111), respectively (see Supporting Information).

Similar to what was observed for a wide range of different molecular species,[6] the TBP molecules tend to self-assemble into compact islands (Figure 2). For both substrates, when scanning at a temperature of 77 K, detachment of individual molecules from the island borders are observed while isolated molecules can be found only at defect sites, suggesting that molecular diffusion is highly activated at room temperature. The size of the TBP islands is, however, very different on the two substrates. On Cu(111), extremely large islands are observed, typically one per terrace (Figure 2a). This may be viewed as the end point of an Ostwald ripening process[7,8] involving molecules that interact through purely attractive van der Waals (vdW) forces. As expected, the average island size grows with the coverage (Figure 2c), and high temperature annealing cycles do not alter the observed assembly, indicating that the system has reached a thermodynamically stable phase. A completely different assembly is found on Au(111) (Figure 2b). In this case, at low coverage (<0.5 MonoLayers, ML), deposition of TBP results in the formation of several small islands, with shapes and sizes that are not significantly determined by the corrugation lines of the herringbone reconstruction but are evenly distributed over the fcc and the hcp areas of the substrate (see Supporting Information).

The high molecular mobility (and the smoother adsorption energy profile expected on the less reactive Au substrate) excludes that any kinetic limitation to diffusion could be responsible for this assembly mode. Moreover, in the case of a kinetics-limited ripening, the average cluster size and density should increase, respectively decrease, with annealing time and temperature.[9,10] However, annealing experiments at different times (up to 20 min) and temperatures (from 320 up to 420 K) produced no changes to the observed arrangement of TBP molecules on Au(111), suggesting that the structures displayed in Figure 2b also correspond to an equilibrium configuration. Thus, our observations point toward a thermodynamic explanation of the assembly observed on Au(111) different from the
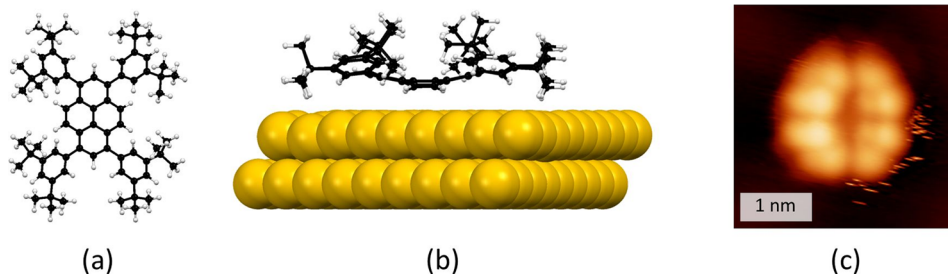

Figure 1. (a) DFT relaxed structure of the TBP molecule in gas phase and (b) adsorbed on the Au(111) surface. (c) Constant current STM image of a TBP molecule adsorbed at a herringbone reconstruction elbow of Au(111). The elbow site induces a slight right–left asymmetry in the adsorption configuration.
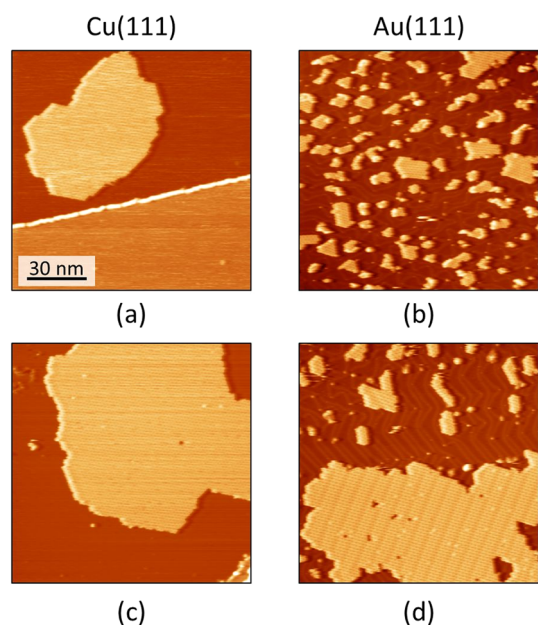
Cu(111)　　　　　　Au(111)

(a)　　　　　　　　(b)

(c)　　　　　　　　(d)

Figure 2. STM images showing the TBP assembly on Cu-(111) and Au(111) surfaces at low (a and b) and high (c and d) molecular coverage, respectively.

standard Ostwald ripening observed on Cu(111) for the same molecule.

For both substrates, DFT calculations show that the molecular projected density of states (pDOS) is essentially unchanged with respect to the gas-phase DOS (Figure SI-6). This physisorption picture is also reflected in rather large adsorption heights, 3.65 and 3.59 Å for Au(111) and Cu(111), respectively (see Supporting Information). Such an adsorption configuration is significantly different from the case of other PAHs, where electronic mixing between molecular orbitals and metal electronic states has been observed.[11,12] However, while on Cu(111) the Fermi level (E_F) is located between the TBP HOMO and LUMO peaks, on Au(111) E_F pins the HOMO which becomes partially unoccupied (Figure SI-6). Although this is a safe indication that TBP acts as an electron donor to Au(111) but not to Cu(111) substrates, the fractional occupancy of the molecular orbitals is likely to be an artifact of the approximated standard functional used in DFT[13,14] and of the ensuing well-known self-interaction error problem (see Supporting Information). In fact, the reduced spatial overlap between molecular and surface wave functions rather points toward an integer charge transfer (ICT)[11,15] mechanism.

To overcome the limitations of DFT, the occurrence of ICT is better assessed by comparing the position of the HOMO energy level relative to E_F. For the adsorbed TBP molecule, the HOMO level can be evaluated by adding to its gas-phase value an "image charge potential" correction that describes the HOMO level upshift due to the electrostatic screening of the metallic substrate[16,17] (see Supporting Information). Meanwhile, the positive intrinsic dipole associated with the

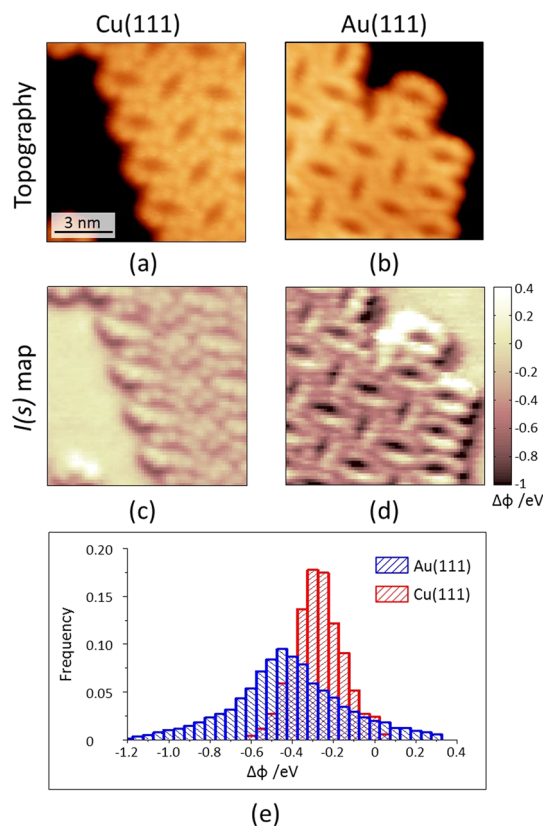Cu(111)　　　　　　Au(111)

(a)　　　　　　　　(b)

(c)　　　　　　　　(d)

(e)

Figure 3. Constant current STM images of TBP molecules deposited on (a) Cu(111) and (b) Au(111). (c and d) Simultaneously acquired local work function maps, showing the variation $\Delta\Phi$ with respect to the clean substrate. (e) The distribution of $\Delta\Phi$ values measured on TBP molecules on Au(111) and Cu(111) are shown in blue and red, respectively.

concave TBP adsorption geometry (Figure 1b) opposes CT, causing a slight HOMO level down-shift (see Supporting Information). By taking both these effects into consideration,[18] the difference between the substrate Fermi level and the modified HOMO of an adsorbed TBP molecule turns out to be $\Delta E_{Au} = -0.18$ eV and $\Delta E_{Cu} = 0.19$ eV for the Au(111) and Cu(111) substrates, respectively. This further supports the DFT prediction that a single TBP molecule is likely to lose one electron upon adsorption on Au(111). The resulting molecular cation would be screened by the electrons in the metal, leading to the formation of an upward pointing, vertical electric dipole (charge transfer dipole). On the other hand, in the case of Cu(111), the TBP molecules should adsorb in their neutral state.

The different propensity of TBP charging on the two metallic substrates was further investigated by scanning tunnelling spectroscopy (STS) measurements of the tunnelling potential barrier Φ[19] (also called "local work function"). Molecular-scale resolved maps of Φ were obtained by measuring $I(s)$ spectra (tunnelling current *versus* tip–sample separation, see Supporting Information) as a function of the lateral tip position[19−21] and are displayed in Figure 3 as variations with respect to the clean substrate ($\Delta\Phi$). Two main features are clearly

Cu(111)   Au(111)

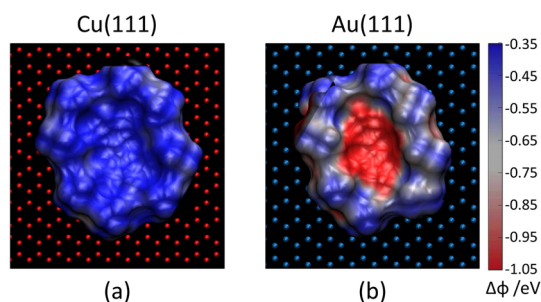(a)   (b)   Δφ /eV

Figure 4. DFT calculated distribution of the electrostatic potential energy shift with respect to the bare substrate for a TBP molecule adsorbed on (a) Cu(111) and (b) Au(111). The values are significantly larger on the molecular core than on the peripheral groups for Au(111) but are uniformly distributed for Cu(111).

evident: negative values of $\Delta\Phi$ over the molecules (Figure 3c,d), the effect being 0.2 eV stronger on Au(111) than on Cu(111) (Figure 3e); a different $\Delta\Phi$ intramolecular contrast on the two substrates, with significant variations (~1 eV) between the 1,3-di(*tert*-butyl)phenyl groups and the pyrene core for TBP on Au(111) (Figure 3d) and a spatially much more uniform $\Delta\Phi$ distribution for TBP on Cu(111) (Figure 3c).

These observations are consistent with an improved energetic stability of positively charged TBP molecules on Au(111) with respect to Cu(111). The smaller Φ values observed in correspondence to the molecular islands on both substrates cannot be directly assigned to charge transfer as they can also be caused by other types of molecular dipoles, including the intrinsic dipole and the so-called *pillow effect*, which all cooperate to reduce the local work function.[1,2,15,17] However, the extra $\Delta\Phi$ drop of ~0.2 eV observed on Au(111) is consistent with an additional contribution to the electrostatic potential caused by a fraction of the deposited molecules being positively charged and thus generating upward pointing ICT molecular dipoles (see Supporting Information).

The stronger intramolecular $\Delta\Phi$ contrast observed on Au(111) further confirms the higher propensity of TBP to get positively charged on this substrate when compared to Cu(111). In fact, although the initial charge state of a physisorbed molecule undergoing reversible ICT will not be preserved when the molecule is traversed by a current of several hundred pA, the Φ map measured at negative sample bias represents the extraction barrier profile experienced by an electron leaving the molecule and moving toward the tip[19] and should thus reflect the higher or lower stability of an electron hole located on the molecule (see Supporting Information). DFT calculations of the electrostatic potential distribution generated by a neutral and a $+e$ charged TBP molecule are shown in Figure 4, panels a and b, respectively (see also Supporting Information). These exhibit an excellent qualitative agreement when compared with the contrast measured in the

experimental $\Delta\Phi$ distribution maps on Cu(111) (Figure 3c) and Au(111) (Figure 3d), respectively.

A coherent picture emerges from our results: Adsorbed TBP molecules remain neutral on Cu(111) and are therefore expected to interact mainly through attractive vdW forces, forming isolated large islands by a standard Ostwald ripening process. On the other hand, TBP molecules adsorbed on Au(111) can host an electric dipole originated by ICT and surface polarization screening. As a consequence, the assembly on Au(111) derives from the coexistence of short-range vdW attraction and long-range repulsive forces between charged molecules. At low coverage, this results in the formation of several small islands uniformly distributed over the surface. At higher coverage, one could expect that the presence of forces of opposite sign acting on different length scales leads to the emergence of peculiar structural motifs (such as striped patterns) as reported in many physical processes,[22] including the formation of magnetic domains, phase separation in block copolymers, pattern development on animal skin and, in a few known cases, 2D supramolecular assembly.[17,23−25] This is however not the case of TBP on Au(111) where, at a coverage higher than about 0.5 ML, the molecules undergo a rather different organization, an *anomalous coarsening*, unusually characterized by the coexistence of small and large islands (Figure 2d). When compared to standard Ostwald ripening, this coarsening is thus *anomalous* in two ways: (1) the formation of several separated small islands instead of a single, large one and (2) the peculiar coverage dependence of the island size distribution.

The formation of large islands upon increasing deposition can only occur if the intermolecular repulsion decreases with coverage. We attribute this to the self-limiting nature of interfacial ICT. According to the well-established ICT picture, the positive dipoles produced by donor molecules generate an electric field that rigidly down-shifts the molecular levels and the vacuum level, with respect to the substrate Fermi energy.[1] As the coverage increases, this reduction of surface work function progresses until no driving force is left to promote further CT and, from this point onward, additional deposited molecules adsorb in their neutral state on the surface.[1,2,15] Although extremely simplified, this picture captures the inherent self-limiting nature of interfacial ICT, by addressing the average monolayer behavior. On a local scale, the driving force ΔE for charging an *individual* molecule depends on the local electric field and thus on the local spatial distribution of already charged molecules. As a consequence, ICT can be inhibited for a molecule close to several already charged neighbors, and charged molecules can reverse back to neutrality if a change in the local molecular arrangement makes this energetically favored. These two processes will occur at an

increasing frequency with increasing molecular coverage, thereby causing the self-limitation of ICT. This inherent interplay between charge transfer and molecular assembly allows a rich repertoire of growth patterns and underpins the normal and anomalous coarsening of TBP on Cu(111) and Au(111), respectively.

To rationalize the observed assembly behavior, we performed equilibrium Monte Carlo (MC) simulations of a simple coarse-grained model where TBP molecules were treated as structure-less particles hosted on a discrete hexagonal lattice. The particles could either be neutral, in which case they only had a small positive dipole representing the intrinsic "conformational" dipole caused by the concave adsorption, or charged, with a larger dipole corresponding to the ICT molecular ion. The charge status of each particle was allowed to reversibly switch between these two states with a MC acceptance rate depending on the total energy variation (see Supporting Information) associated with the switch. Each charged particle contributed an energy term corresponding to the difference between the TBP HOMO level and the substrate E_F, which, according to our previous calculations, is positive for Cu(111) and negative for Au(111). Negative short-range interaction terms associated with nearest neighbors attraction and positive $\sim 1/r^3$ terms acting between each pair of molecules were also included in the model Hamiltonian to represent the vdW interactions and the dipole–dipole long-range repulsion, respectively.

The model predicts neutral adsorption for all TBP molecules on Cu(111). For this system, low coverage (0.2–0.3 ML) simulations yield a stable assembly into a single large island (Figure 5a), consistent with what we observe experimentally (Figure 2a). However, a very different growth pattern develops on Au(111) (Figure 5b), with molecules arranged in several small islands, closely reflecting our low coverage observations (Figure 2b). Thus, taking into account the repulsive interactions, the formation of CT dipoles is both necessary and sufficient to reproduce the assembly behavior observed on Au(111) (Figure 2b). At higher coverage (>0.4 ML), the model predicts the coexistence of small and large clusters (Figure 5d) in very good agreement with the experiments (Figure 2d). This result is a direct consequence of incorporating reversible, coverage dependent ICT into the model. Indeed, by allowing each TBP molecule to access both the charged and the neutral state, local crowding of charged molecules can be allowed in small islands and avoided inside large islands. In both these coexisting structures the density of charged molecule reflects the optimal local balance between maximizing CT energy gain and minimizing the total electrostatic repulsion. Conversely, if irreversible CT is imposed by enforcing the charging of all particles, the model predicts a very different high-coverage behavior, i.e., the formation of striped phases (cf. Figure SI-8a).[22]

Cu(111)   Au(111)
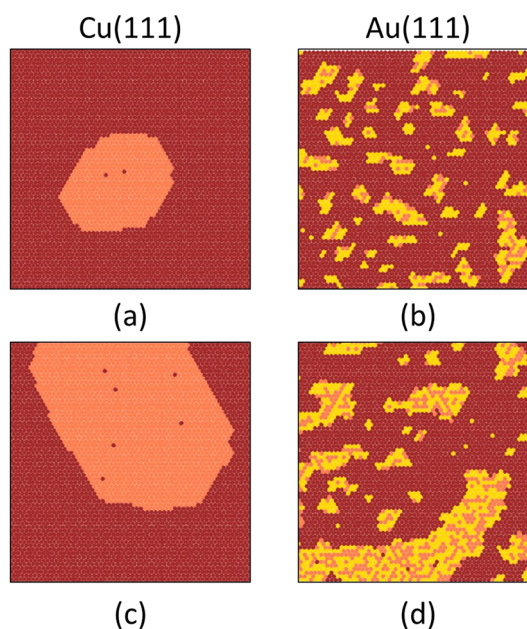
(a)   (b)

(c)   (d)

Figure 5. Monte Carlo simulation snapshots of the TBP self-assembly on Cu and Au substrates, obtained allowing only neutral molecules (left panels), or both charged and neutral species (right panels). Neutral and charged molecules are represented in yellow and pink colors; top and bottom panels correspond to low and high coverage, respectively.

We believe that our analysis of the inter-relation between supramolecular assembly and reversible charge transfer has a much wider applicability than the TBP on Au(111) system. Indeed, several examples can be found in the literature, where the assembly of functional molecular units was reported to follow an anomalous coarsening.[26–28] However, to the best of our knowledge, this phenomenon was not directly addressed or properly explained so far. Our work can help rationalize similar observations and identify the precise conditions that the molecular units and the substrate must meet in order for anomalous coarsening to occur. Namely, the selected monomers must get ionized as a result of CT while the short-range vdW attraction between monomers must be such that assembly is significantly moderated, while not forbidden, by the energy cost associated with long-range electrostatic repulsion. This requires a careful balance of the monomer's properties such as lateral size, intrinsic dipole, and adsorption height over the surface (see Supporting Information). Anomalous coarsening can happen at this point under the further key condition that reversible charging is possible. This is clearly not the case of, e.g., irreversible deprotonation[29] or surface-induced aromatic stabilization through the formation of molecule–substrate covalent bonds.[30] At low coverage, the optimal arrangement will be achieved by limiting the assembly to small islands. If a higher coverage is forced by further deposition, some much larger stable islands will be able to form, with a fraction of the molecules reverting to a neutral
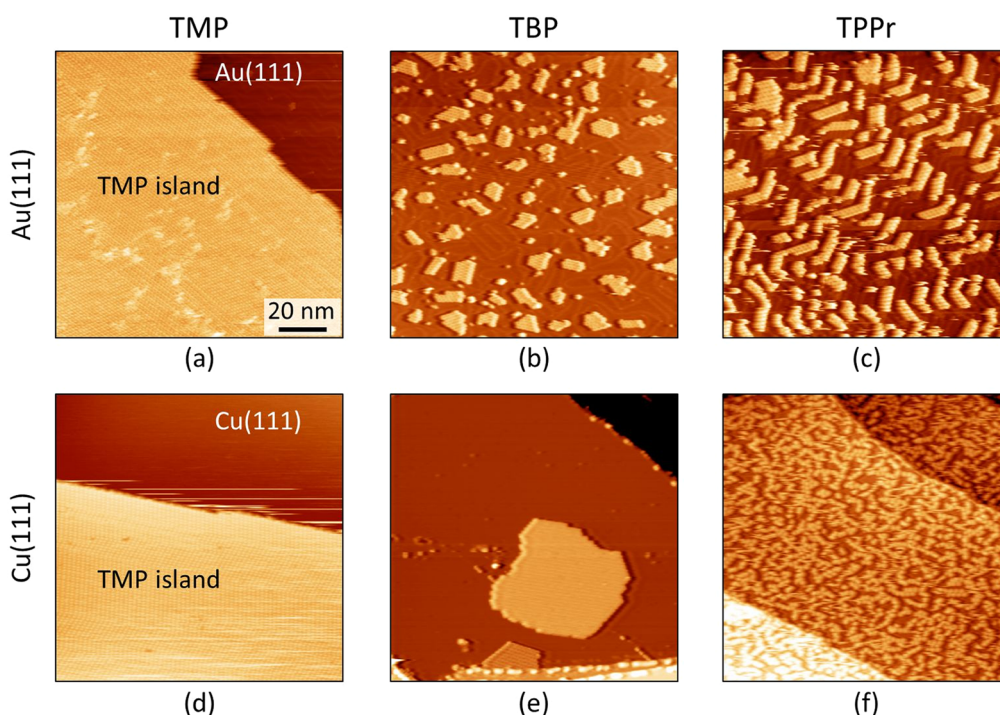
Figure 6. STM images showing the assembly of TMP, TBP and TPPr molecules on Au(111) and Cu(111) surfaces.

state while remaining interdispersed with the charged ones.

The occurrence of *normal* and *anomalous coarsening* in the assembly of TBP on Cu(111) and Au(111), respectively, results from the inhibition or enabling of ICT at the metal−organic interface obtained by changing the work function of the substrate ($\Phi_{Cu(111)}$ = 4.9 eV and $\Phi_{Au(111)}$ = 5.3 eV). However, since to a first approximation ICT is linked to the relative position of the HOMO level with respect to the metallic Fermi energy, another strategy to obtain the same effect is to modify the HOMO by engineering appropriate molecular modules. To investigate this way to control the self-assembly, we synthesized two further molecules: 1,3,6,8-tetramesitylpyrene (TMP) and 2,5,8,11-tetrakis-(3,5-di*tert*-butylphenyl)perylene (TPPr) (see Supporting Information). The peripheral mesityl groups of TMP and the extended perylene core of TPPr were selected as they should significantly affect the adsorption height of the two central polyaromatic cores, making it respectively higher and lower than that of TBP. As a consequence, the image charge potential correction describing the HOMO level upshift on metallic substrates is expected to be higher and lower for TPPr and TMP, respectively, when compared to TBP. This should influence the ICT process on the Au(111) and Cu(111) substrates and thus have a noticeable effect on the 2D self-assembly.

Figure 6 shows the experimentally observed assemblies obtained after room temperature deposition of TMP, TBP and TPPr on Au(111) and Cu(111) (STM images acquired at 77 K). As for TBP, the high molecular

mobility observed for TMP and TPPr at 77 K and the fact that island size distributions do not change after thermal annealing cycles indicate that all the structures in Figure 6 correspond to thermodynamically stable phases. TMP molecules aggregate in large and compact islands on both metals and their assembly follows a normal coarsening. This is an indication that, due to the large adsorption height of TMP and the ensuing small image charge potential correction to the HOMO, no charge transfer is taking place on either substrate. On the contrary, even if the island sizes and shapes formed by TPPr on Au(111) are significantly influenced by the herringbone reconstruction (see Supporting Information), it is evident that TPPr displays anomalous coarsening on both metals, showing that repulsive intermolecular forces are present on both metal−organic interfaces. We interpret this as the direct consequence of the smaller adsorption height of TPPr compared with that of TBP, induced by its flatter structure (see Figure SI-5). This causes a larger image charge correction for the HOMO and thus allows the CT process also on Cu(111). Finally, as already described, TBP shows an intermediate behavior between TMP and TPPr, with an anomalous coarsening indicative of CT on the higher work function Au(111) surface and a normal coarsening typical of neutral molecules on the less noble Cu(111).

CONCLUSIONS

In the present work, *ad hoc* synthesized tetra-legged pyrene derivatives (TBP) were designed to weakly interact with transition metal substrates and such that

their effective ionization potential is smaller than the substrate work function but very close to it. When deposited on the Au(111) surface, these molecular units follow a novel growth mode characterized by anomalous coarsening. The specifically chosen characteristics of this model metal−organic interface have allowed us to identify the causes of the anomalous coarsening as the interplay between intermolecular repulsion, caused by reversible integer charge transfer, and van der Waals attraction. On the basis of this insight, further tetra-legged π-conjugated molecules

(TPPr and TMP) were prepared to specifically enable or inhibit interfacial charge transfer. The coherence of our findings was then demonstrated by verifying that their assembly on metal substrates with different work functions followed anomalous or normal coarsening, respectively. We speculate that, even if possibly less clearly discernible, the same mechanisms should be operating in a wide range of metal−organic interfaces based on functional PAHs, and should thus be considered when investigating their two-dimensional assembly.

METHODS

Experimental Methods. The molecular structures were investigated with a commercial LT-STM operated in ultrahigh vacuum at a temperature of 77 K. Cu(111) and Au(111) single crystals were cleaned by multiple cycles of Ar$^+$ sputtering (1 keV) and annealing (up to 800 K). After several hours of degassing, TMP, TBP, TPPr molecules were deposited by means of organic molecular beam epitaxy (OMBE) at different coverages onto the substrates held at 300 K. STM images were acquired at 77 K using electrochemically etched tungsten tips. Typical values for bias voltage and tunnelling current were −2 V (occupied state imaging) and 20 pA, respectively. The spatial variations of the local work function were measured at 5 K by adding a sinusoidal modulation voltage to the z-piezo of the STM *via* an external lock-in amplifier and recording the output of the lock-in tuned on the first harmonic. Measurements were done in closed feedback loop conditions during constant current scanning with typical modulation frequencies of 3−5 kHz (always higher than the cutoff frequency of the feedback loop) and peak-to-peak amplitudes of 0.2−0.6 Å. For further details see the Supporting Information. All the STM images were processed by using the WSxM software.[31]

Computational Methods. Density functional theory (DFT) calculations were performed with the plane-wave-pseudo potential package Quantum-ESPRESSO,[32] using ultrasoft pseudopotentials[33] and a PBE-GGA exchange-correlation (*xc*) functional[13] modified by the self-consistent DF-vdW functional,[34] to account for vdW interactions. Gas-phase and on the substrate relaxations were performed with a wave function energy cutoff of 408 and 204 eV, respectively. Charge transfer self-consistent calculations on the substrate were recomputed using 408 eV. Brillouin-zone sampling included the $\mathbf{k} = \Gamma$ point only. The Makov−Payne correction[35] was added to charged molecule total energies, while a counter dipole term[36,37] was included in surface calculations. Au(111) and Cu(111) surfaces were modeled with a slab containing two layers, allowing a vacuum (ad-layer surface distance) of ∼10 Å. Forces were relaxed up to 0.26 eV/Å. Only forces acting on the top layer and the ad-layer atoms were relaxed.

Synthetic Methods. *1,3,6,8-Tetrakis(3,5-di-tert-butylphenyl)-pyrene (TBP).* 2-(3,5-Di-*tert*-butylphenyl)-4,4,5,5-tetramethyl-[1,3,2]dioxaborolane[38] (1 g, 3.16 mmol), 1,3,6,8-tetrabromopyrene[39] (200 mg, 0.39 mmol), and Pd(PPh$_3$)$_4$ (22.4 mg, 0.02 mmol) were added to a 25 mL microwave vial. Cs$_2$CO$_3$ (1.1 g, 3.1 mmol) was dissolved in 2.5 mL of EtOH and 2.5 mL of DMF. The resulting mixture was transferred to the vial, and 5 mL of toluene was added. H$_2$O (2 drops) was finally added, and the resulting mixture was put under microwave for 4 h at 80 °C. The resulting mixture was dissolved in Et$_2$O (10 mL). The organic layer was then washed with water (2 × 20 mL). The aqueous phase was washed with Et$_2$O (2 × 20 mL). The organic layers were collected, dried over MgSO$_4$, filtered and evaporated to dryness. The crude was purified by column chromatography using pentane as eluent. TBP was obtained as a white solid (244 mg, 67%). Mp: 123−125 °C. IR (cm^{-1}): ν 2962.97, 1593.92, 1476.12, 1362.25, 1247.39, 1021.30, 876.97, 817.89, 717.02. UV−vis (C$_6$H$_{12}$, rt): λ_{max} (nm) = 388; ε_{max} (mol^{-1} L cm^{-1}) = 11665.2,

λ_{max} (nm) = 299; ε_{max} (mol^{-1} L cm^{-1}) = 16065.8. ^{1}H NMR (400 MHz, C$_6$D$_6$): δ 8.58 (s, 4H, Ar*H*), 8.47 (s, 2H, Ar*H*), 7.76 (d, *J* = 1.48 Hz, 8H, Ar*H*), 7.65 (t, *J* = 1.48 Hz, 4H, Ar*H*), 1.30 (s, 72H, CC*H*$_3$); ^{13}C NMR (400 MHz, CDCl$_3$): δ 150.81, 140.44, 138.14, 129.56, 128.18, 126.37, 125.40, 121.25, 35.20, 31.75. MALDI-HRMS: calcd 954.7043, *m/z*: 954.7053 ([M]$^+$, C$_{72}$H$_{90}$$^+$).

1,3,6,8-Tetrakis(2,4,6-trimethylphenyl)pyrene (TMP). To a 5 mL microwave vial was added mesitylboronic acid[40] (500 mg, 3.04 mmol), 1,3,6,8-tetrabromopyrene (100 mg, 0.19 mmol), Pd$_2$(dba)$_3$ (2.4 mg, 0.002 mmol), S-Phos (2.05 mg, 0.004 mmol) and K$_3$PO$_4$ (580 mg, 2.73 mmol). Dry toluene (5 mL) was then added, and the mixture was stirred at the microwave for 16 h at 100 °C. The resulting mixture was dissolved in CH$_2$Cl$_2$. The organic layer was then extracted with H$_2$O (2 × 20 mL), and the resulting aqueous phase was then extracted with CH$_2$Cl$_2$ (2 × 20 mL). The combined organic layers were dried over MgSO$_4$ and evaporated *in vacuo*. The residue was purified by precipitation−recrystallization in EtOAc to afford TMP as a white solid (105 mg, 68%). C$_{52}$H$_{50}$, MW: 674.95 g/mol. Mp > 250 °C. IR (cm^{-1}): ν 568.19, 616.29, 731.7, 819.7, 837.56, 850.21, 906.3, 1005.57, 1376.73, 1437.14, 1458.62, 1475.93, 1610.9, 2916.39, 2967.54. UV−vis (CH$_2$Cl$_2$, rt): λ_{max} (ε_{max}, mol^{-1} L cm^{-1}) 253 (85182), 288 (75571), 346 (51278), 363 (64098). δ_H(400 MHz, CDCl$_3$) 7.60 (s, 2H, Ar*H*), 7.52 (s, 4H, Ar*H*), 7.01 (s, 8H, Ar*H*), 2.39 (s, 12H, C*H*$_3$), 1.95 (s, 24H, C*H*$_3$). δ_C (400 MHz, CDCl$_3$) 137.30, 136.91, 136.35, 129.16, 128.57, 128.20, 126.01, 124.92, 21.30, 20.87 (one peak is missing probably due to overlap). MALDI-HRMS: calcd 697.3805, *m/z*: 697.3808 ([M + Na]$^+$ C$_{52}$H$_{50}$ + Na$^+$).

2,5,8,11-Tetrakis(3,5-di-tert-butylphenyl)perylene (TPPr). To a 5 mL microwave vial was added 1-bromo-3,5-di-*tert*-butylphenyl (285 mg, 1.05 mmol), 2,5,8,11-tetrakis(4,4,5,5-tetramethyl-1,3,2-dioxaborolan-2-yl)perylene[41] (100 mg, 0.13 mmol) and Pd(PPh$_3$)$_4$ (8 mg, 0.007 mmol). Cs$_2$CO$_3$ (345 g, 1.05 mmol) was dissolved in a mixture of EtOH/DMF 1:1 mL. The resulting mixture was transferred to the vial, and 2 mL of toluene was added. H$_2$O (2 drops) were finally added, and the resulting mixture was placed under microwave for 2 h at 80 °C. The resulting mixture was dissolved in Et$_2$O. The organic layer was then washed with H$_2$O (2 × 20 mL), and the resulting aqueous phase was extracted with Et$_2$O (2 × 20 mL). The combined organic layers were dried over MgSO$_4$ and evaporated *in vacuo*. The crude was then purified by column chromatography using cyclohexane as eluent with a gradient of (cyclohexane/CH$_2$Cl$_2$, 9:1) affording desired TPPr as a pale yellow solid (17 mg, 13%). C$_{76}$H$_{92}$, MW: 1005.54 g/mol. Mp > 250 °C. IR (cm^{-1}): ν 712.34, 739.17, 800.20, 867.29, 1019.72, 1088.86, 1248.43, 1260.50, 1362.09, 1393.01, 1476.49, 1594.85, 2866.66, 2903.52, 2960.86. UV−vis (CH$_2$Cl$_2$, rt): λ_{max} (ε_{max}, mol^{-1} L cm^{-1}) 402 (8567), 426 (18494), 454 (26112). δ_H (400 MHz, CDCl$_3$) 8.57 (s, 4H, Ar*H*), 8.01 (s, 4H, Ar*H*), 7.69 (d, *J* = 1.83 Hz, 8H, Ar*H*), 7.53 (t, *J* = 1.83 Hz, 4H, Ar*H*), 1.46 (s, 72H, Ar*H*). δ_C (400 MHz, CDCl$_3$) 151.57, 140.81, 140.58, 135.72, 131.58, 127.34, 126.37, 121.94, 120.54, 35.25, 31.77 (one peak is missing probably due to overlap). MALDI-HRMS: calc. 1004.7194, *m/z*: 1004.6963 ([M]$^+$ C$_{76}$H$_{92}$$^+$).

Conflict of Interest: The authors declare no competing financial interest.

Supporting Information Available: Details of the molecular synthesis, the sample preparation, the scanning tunnelling microscopy and spectroscopy characterization, the density functional theory and the equilibrium Monte Carlo simulations. This material is available free of charge *via* the Internet at http://pubs.acs.org.

REFERENCES AND NOTES

1. Ishii, H.; Sugiyama, K.; Ito, E.; Seki, K. Energy Level Alignment and Interfacial Electronic Structures at Organic/Metal and Organic/Organic Interfaces. *Adv. Mater.* **1999**, *11*, 605–625.

2. Braun, S.; Salaneck, W. R.; Fahlman, M. Energy-Level Alignment at Organic/Metal and Organic/Organic Interfaces. *Adv. Mater.* **2009**, *21*, 1450–1472.

3. Harada, M.; Ohga, Y.; Watanabe, I.; Watarai, H. Ionization Energies for Solvated Polycyclic Aromatic Hydrocarbons. *Chem. Phys. Lett.* **1999**, *303*, 489–492.

4. Holm, A. I. S.; Johansson, H. A. B.; Cederquist, H.; Zettergren, H. Dissociation and Multiple Ionization Energies for Five Polycyclic Aromatic Hydrocarbon Molecules. *J. Chem. Phys.* **2011**, *134*, 044301-1–044301-7.

5. Crocker, L.; Wang, T.; Kebarle, P. Electron Affinities of Some Polycyclic Aromatic Hydrocarbons, Obtained from Electron-Transfer Equilibria. *J. Am. Chem. Soc.* **1993**, *115*, 7818–7822.

6. Barth, J. V. Molecular Architectonic on Metal Surfaces. *Annu. Rev. Phys. Chem.* **2007**, *58*, 375–407.

7. Voorhees, P. W. The Theory of Ostwald Ripening. *J. Stat. Phys.* **1985**, *38*, 231–252.

8. Ostwald, W. *Lehrbuch Der Allgemeinen Chemie*; W. Engelmann: Leipzig, 1896.

9. Chakraverty, B. K. Grain Size Distribution in Thin Films—1. Conservative Systems. *J. Phys. Chem. Solids* **1967**, *28*, 2401–2412.

10. Wynblatt, P.; Gjostein, N. A. Supported Metal Crystallites. *Prog. Solid State Chem.* **1975**, *9*, 21–58.

11. Bussolotti, F.; Friedlein, R. Hybridization and Charge Transfer at the Anthracene/Cu(110) Interface: Comparison to Pentacene. *Phys. Rev. B* **2010**, *81*, 115457-1–115457-7.

12. Ferretti, A.; Baldacchini, C.; Calzolari, A.; Di Felice, R.; Ruini, A.; Molinari, E.; Betti, M. G. Mixing of Electronic States in Pentacene Adsorption on Copper. *Phys. Rev. Lett.* **2007**, *99*, 046802-1–046802-4.

13. Perdew, J. P.; Burke, K.; Ernzerhof, M. Generalized Gradient Approximation Made Simple. *Phys. Rev. Lett.* **1996**, *77*, 3865–3868.

14. Dreizler, R. M.; Gross, E. K. E. K. U. *Density Functional Theory: An Approach to the Quantum Many-Body Problem*; Springer-Verlag: Berlin, 1990.

15. Fahlman, M.; Crispin, A.; Crispin, X.; Henze, S. K. M.; de Jong, M. P.; Osikowicz, W.; Tengstedt, C.; Salaneck, W. R. Electronic Structure of Hybrid Interfaces for Polymer-Based Electronics. *J. Phys.: Condens. Matter.* **2007**, *19*, 183202-1–183202-20.

16. Neaton, J. B.; Hybertsen, M. S.; Louie, S. G. Renormalization of Molecular Electronic Levels at Metal-Molecule Interfaces. *Phys. Rev. Lett.* **2006**, *97*, 216405-1–216405-4.

17. Tomba, G.; Stengel, M.; Schneider, W.-D.; Baldereschi, A.; De Vita, A. Supramolecular Self-Assembly Driven by Electrostatic Repulsion: The 1D Aggregation of Rubrene Pentagons on Au(111). *ACS Nano* **2010**, *4*, 7545–7551.

18. Smith, F. T. Capacitive Energy and the Ionization of Aromatic Hydrocarbons. *J. Chem. Phys.* **1961**, *34*, 793–801.

19. Vitali, L.; Levita, G.; Ohmann, R.; Comisso, A.; De Vita, A.; Kern, K. Portrait of the Potential Barrier at Metal-Organic Nanocontacts. *Nat. Mater.* **2010**, *9*, 320–323.

20. Binnig, G.; Rohrer, H. Scanning Tunneling Microscopy. *Surf. Sci.* **1983**, *126*, 236–244.

21. Rojas, G.; Simpson, S.; Chen, X. M.; Kunkel, D. A.; Nitz, J.; Xiao, J.; Dowben, P. A.; Zurek, E.; Enders, A. Surface State Engineering of Molecule-Molecule Interactions. *Phys. Chem. Chem. Phys.* **2012**, *14*, 4971–4976.

22. Seul, M.; Andelman, D. Domain Shapes and Patterns—The Phenomenology of Modulated Phases. *Science* **1995**, *267*, 476–483.

23. Fraxedas, J.; Garcia-Gil, S.; Monturet, S.; Lorente, N.; Fernandez-Torrente, I.; Franke, K. J.; Pascual, J. I.; Vollmer, A.; Blum, R. P.; Koch, N.; *et al.* Modulation of Surface Charge Transfer through Competing Long-Range Repulsive *versus* Short-Range Attractive Interactions. *J. Phys. Chem. C* **2011**, *115*, 18640–18648.

24. Blum, M. C.; Cavar, E.; Pivetta, M.; Patthey, F.; Schneider, W. D. Conservation of Chirality in a Hierarchical Supramolecular Self-Assembled Structure with Pentagonal Symmetry. *Angew. Chem., Int. Ed.* **2005**, *44*, 5334–5337.

25. Jewell, A. D.; Simpson, S. M.; Enders, A.; Zurek, E.; Sykes, E. C. H. Magic Electret Clusters of 4-Fluorostyrene on Metal Surfaces. *J. Phys. Chem. Lett.* **2012**, *3*, 2069–2075.

26. Gross, L.; Moresco, F.; Ruffieux, P.; Gourdon, A.; Joachim, C.; Rieder, K. H. Tailoring Molecular Self-Organization by Chemical Synthesis: Hexaphenylbenzene, Hexa-Peri-Hexabenzocoronene, and Derivatives on Cu(111). *Phys. Rev. B* **2005**, *71*, 165428−1−165428−7.

27. Yokoyama, T.; Yokoyama, S.; Kamikado, T.; Mashiko, S. Nonplanar Adsorption and Orientational Ordering of Porphyrin Molecules on Au(111). *J. Chem. Phys.* **2001**, *115*, 3814–3818.

28. Écija, D.; Trelka, M.; Urban, C.; Mendoza, P. d.; Mateo-Martí, E.; Rogero, C.; Martín-Gago, J. A.; Echavarren, A. M.; Otero, R.; Gallego, J. M.; *et al.* Molecular Conformation, Organizational Chirality, and Iron Metalation of Meso-Tetramesitylporphyrins on Copper(100). *J. Phys. Chem. C* **2008**, *112*, 8988–8994.

29. Kervyn, S.; Kalashnyk, N.; Riello, M.; Moreton, B.; Tasseroul, J.; Wouters, J.; Jones, T. S.; De Vita, A.; Costantini, G.; Bonifazi, D. "Magic" Surface Clustering of Borazines Driven by Repulsive Intermolecular Forces. *Angew. Chem., Int. Ed.* **2013**, *52*, 7410–7414.

30. Heimel, G.; Duhm, S.; Salzmann, I.; Gerlach, A.; Strozecka, A.; Niederhausen, J.; Burker, C.; Hosokai, T.; Fernandez-Torrente, I.; Schulze, G.; *et al.* Charged and Metallic Molecular Monolayers through Surface-Induced Aromatic Stabilization. *Nat. Chem.* **2013**, *5*, 187–194.

31. Horcas, I.; Fernandez, R.; Gomez-Rodriguez, J. M.; Colchero, J.; Gomez-Herrero, J.; Baro, A. M. Wsxm: A Software for Scanning Probe Microscopy and a Tool for Nanotechnology. *Rev. Sci. Instrum.* **2007**, *78*, 013705-1–013705-8.

32. Giannozzi, P.; Baroni, S.; Bonini, N.; Calandra, M.; Car, R.; Cavazzoni, C.; Ceresoli, D.; Chiarotti, G. L.; Cococcioni, M.; Dabo, I.; *et al.* Quantum Espresso: A Modular and Open-Source Software Project for Quantum Simulations of Materials. *J. Phys.: Condens. Matter.* **2009**, *21*, 395502-1–395502-19.

33. Vanderbilt, D. Soft Self-Consistent Pseudopotentials in a Generalized Eigenvalue Formalism. *Phys. Rev. B* **1990**, *41*, 7892–7895.

34. Dion, M.; Rydberg, H.; Schroder, E.; Langreth, D. C.; Lundqvist, B. I. Van der Waals Density Functional for General Geometries. *Phys. Rev. Lett.* **2004**, *92*, 246401-1–246401-4.

35. Makov, G.; Payne, M. C. Periodic Boundary Conditions in *ab Initio* Calculations. *Phys. Rev. B* **1995**, *51*, 4014–4022.

36. Bengtsson, L. Dipole Correction for Surface Supercell Calculations. *Phys. Rev. B* **1999**, *59*, 12301–12304.

37. Neugebauer, J.; Scheffler, M. Adsorbate-Substrate and Adsorbate-Adsorbate Interactions of Na and K Adlayers on Al(111). *Phys. Rev. B* **1992**, *46*, 16067–16080.

38. Ranta, J.; Kumpulainen, T.; Lemmetyinen, H.; Efimov, A. Synthesis and Characterization of Monoisomeric 1,8,15,22-Substituted (A3b and A2b2) Phthalocyanines and Phthalocyanine−Fullerene Dyads. *J. Org. Chem.* **2010**, *75*, 5178–5194.

39. Venkataramana, G.; Sankararaman, S. Synthesis, Absorption, and Fluorescence-Emission Properties of 1,3,6,8-Tetraethynylpyrene and Its Derivatives. *Eur. J. Org. Chem.* **2005**, *2005*, 4162–4166.

40. Wipf, P.; Jung, J. K. Formal Total Synthesis of (+)-Diepoxin Sigma. *J. Org. Chem.* **2000**, *65*, 6319–6337.

41. Coventry, D. N.; Batsanov, A. S.; Goeta, A. E.; Howard, J. A. K.; Marder, T. B.; Perutz, R. N. Selective Ir-Catalysed Borylation of Polycyclic Aromatic Hydrocarbons: Structures of Naphthalene-2,6-bis(boronate), Pyrene-2,7-bis(boronate) and Perylene-2,5,8,11-tetra(boronate) Esters. *Chem. Commun.* **2005**, *16*, 2172–2174.